Journal of Molecular Liquids 369 (2023) 120791

Contents lists available at ScienceDirect

Journal of Molecular Liquids

journal homepage: www.elsevier.com/locate/molliq

Lipid nanoparticles with erythrocyte cell-membrane proteins

Attila Bóta [a,*], Bence Fehér [b,*], András Wacha [a], Tünde Juhász [a], Dániel Szabó [a], Lilla Turiák [a], Anikó Gaál [a], Zoltán Varga [a], Heinz Amenitsch [c], Judith Mihály [a]

[a] Research Centre for Natural Sciences, Institute of Materials and Environmental Chemistry, Magyar tudósok körútja 2, 1117 Budapest, Hungary
[b] Laboratory of Self-Organizing Soft Matter, Department of Chemical Engineering and Chemistry, Eindhoven University of Technology, P.O. Box 513, 5600 MB Eindhoven, the Netherlands
[c] Austrian SAXS beamline@ELETTRA, Are Science Park 34149 Basovizza TS, Trieste, Italy and Inorganic Chemistry, Graz University of Technology, Stremayrgasse 9, 8010 Graz, Austria

ARTICLE INFO

Article history:
Received 29 July 2022
Revised 7 November 2022
Accepted 8 November 2022
Available online 13 November 2022

Keywords:
Nanoparticles
Nanoerythrosomes
Protein-lipid assembly
Secondary structure
Protein-to-lipid ratio
Protein mass-pattern

ABSTRACT

When the separated erythrocyte membranes (known as ghosts) are ultrasonicated, a significant part of the membrane proteins are released in the aqueous solvent, instead of being incorporated into the membranes of the formed nanoerythrosomes. In contrast to their membrane-bound counterparts, where helices and β-strands dominate, the released proteins show perturbed secondary structures with an increased ratio of helices, presumably participating in molten globules, as it has been revealed by circular dichroism (CD) and infra-red spectroscopy (IR). The shape and size of these proteins is diverse, and even their aggregates appear. When excess lipid (palmitoyl-lysophosphatidylcholine, LPC) is added to different ghost-derivatives (the full nanoerythrosome system, and its ultracentrifugation pellet and supernatant) in 2 × and 5 × lipid-to-protein mass ratio, various lipid nanoparticles are produced. The core–shell and nanodisc structural models obtained by small-angle X-ray scattering (SAXS) indicate that the choice of the precursor system has a more prominent effect on the resulting shape than the amount of lipid added: when starting from the protein-rich supernatant fraction, small (approx. 5 nm high and 7 nm wide) nanodisks are created. When lipid membranes are already present (in the pellet and the full nanoerythrosome fraction), similar LPC addition results in prolate ellipsoidal particles, with an aspect ratio between 3 and 5, and decreasing overall size when the amount of added lipid is increased. The ellipsoids formed from the total nanoerythrosome fraction are smaller than those from the ultracentrifugation pellet (longest axis around 15 *vs* 26 nm), whereas for higher LPC-to-protein ratio, the size in both cases reduce to nearly the same (13–14 nm) in both cases.

1. Introduction

In the last decade biocompatible nanoparticles containing pharmaceutical macromolecules (e.g. mRNA-containing COVID-19 vaccines, nanovehicles of monoclonal antibodies etc.) acquired much importance, due to their high potential for tailored targeting and efficiency in drug delivery [1–4]. The size reduction of such nanovehicles, even of those achieved by lipid nanoparticles, plays a crucial role in cancer treatment as the enhanced permeation and retention (EPR) effect of the tumour tissue requires that the size of the nanocarrier formulation of the anticancer drug should be significantly below 100 nm, even for active targeting cases [5,6].

In order to increase the biocompatibility of traditional nanocarriers, such as inorganic nanoparticles, erythrocyte ghosts, i.e. separated membranes of red blood cells, are frequently used to add a "cloak of invisibility" to synthesized particles [7]. Ghost membranes, just by themselves, can also be transformed to highly biocompatible unilamellar spherical shells by ultrasonication and/or extrusion. These protein-decorated vesicle like formations, known as nanoerythrosomes, one of the most favoured nanocarriers for drug or dye molecules in the field of medical treatment and diagnostics [8–14]. Although the proteins of ghosts, and also nanoerythrosomes, play an important role in the reduction of immune responsibility, these inevitable components are less studied and their structural/functional impact is still not fully understood [15,16].

When nanoerythrosomes are produced from ghosts by ultrasonication, a significant number of proteins is released from the membranes into the solvent phase. Interestingly, although the protein-to-lipid ratio of nanoerythrosomes this way becomes less than the original ghost membranes, but the protein pattern remains highly similar to that of the precursor [10,16].

* Corresponding authors.
E-mail addresses: bota.attila@ttk.hu (A. Bóta), b.feher@tue.nl (B. Fehér).

https://doi.org/10.1016/j.molliq.2022.120791
0167-7322/

By adding membrane-analogous artificial lipids to ghost under ultrasonication, nanoerythrosomes are still formed, but they show peculiar surface morphologies and more extended size ranges, which can be controlled by the amount and kind of added artificial lipids [16]. Especially lysophospholipids play a decisive role in the size reduction of the nanoerythrosomes. On the other hand, these "biosurfactants" are natural metabolites, with important roles as markers in connection with several diseases [17]. They can interact with receptors as well as enzymes and can cause alterations in cell-mechanisms[18–20]. Here we show that lysophospholipids easily associate with proteins and can collect the solubilized proteins, which might be used as a useful alternative approach when handling protein-containing systems. The addition of lysophospholipid (palmitoyl- phosphocholine, LPC) to different fractions of nanoerythrosomes results in different nanoparticle formations. The structural characterization of these nano-objects is in the focus of the present work.

Characterisation of small nanoparticles is generally difficult, especially in the small size-range (below approx. 100 nm) [21]. Visual information, frequently obtained by the means of cryo-EM or transmission electron-microscopy (TEM) combined with freeze-fracture (FF), is very important for revealing morphology, but its statistical relevance is generally low and prone to human bias. Furthermore, even if it is assumed that the native structure is retained during sample preparation, these methods are unfortunately not suitable in the case of small nanoparticles (less than 50 nm), because of their limited resolution. In the complex physico-chemical study of the presented, nanoerythrosome-based protein-lipid nanoparticles, among the different experimental methods, small-angle X-ray scattering turned out to be a powerful tool.

2. Materials and methods

2.1. Chemicals

Physiological salt solution (9 g NaCl dissolved in 991 g Millipore water) was used for erythrocyte isolation. Hypotonic TRIS buffer was the medium of membrane preparation (7.5 mM TRIS, pH 7.6). The final buffer for haemoglobin-free ghost membranes was PBS (10 mMolar; 8 g NaCl, 0.2 g KCl, 1.8 g $Na_2HPO_4{\cdot}2H_2O$, 0.312 g $NaH_2PO_4{\cdot}2H_2O$ for 1 L PBS solution, the final pH value was adjusted to 7.4 by HCl). All listed salts were purchased from Sigma Aldrich. LPC (1-palmitoyl-2-hydroxy-*sn-glycero*-3-phosphocholine) was purchased from Avanti Polar Lipids. All chemicals were used without further purification.

2.2. Ghost and nanoerythrosome preparation protocol

Freshly collected anticoagulated blood was donated by healthy volunteers, two times, 18 ml from one donor at a time. For blood collection 6 ml K_3EDTA tubes were used (Vacuette, Greiner Bio-One, Austria). The use of human blood samples was approved by the Scientific Ethics Committee of the Hungarian Health Scientific Council (ETT TUKEB 6449–2/2019).

Cellular components were sedimented from whole blood by centrifugation at 2500 × g for 10 min in a swing-out rotor (Nüve NF 800R centrifuge). Plasma and the white blood cell-containing buffy coat were removed, and the erythrocyte pellet was suspended in physiological NaCl solution and washed three times. After the last sedimentation, the red blood cells were lysed in hypotonic TRIS buffer (7.5 mM, pH = 7.6), stirred in 40 × buffer volume at 4 °C for half an hour. The erythrocyte ghost membrane was sedimented with an Avanti J26XP centrifuge in a JA-14 fixed angle rotor at an average 13 900 × g for 1 h at 4 °C. To achieve haemoglobin-free ghosts, the membrane pellet was suspended in TRIS buffer, washed two times, and thirdly with PBS buffer. For the separation a Thermo Sorwall WX ultracentrifuge was used with a T-1270 fixed angle rotor, at an average 22 200 × g, for 30 min, at 4 °C.

The final ghost membrane pellet was suspended in PBS, yielding approx. 2 w(weight)/v(volume) % concentration. The protein content of this suspension (abbreviated in the following as GHOST) was determined by Bradford protein assay and was used as a stock solution for nanoerythrosome preparation. The ghost membrane aliquots were rapidly frozen and stored in liquid nitrogen until further use.

Nanoerythrosomes (abbreviated as NERY) were obtained from the ghost membrane suspension (typically, 500 μl) in 1.5 ml glass vials by sonication in a bath sonicator (Elmasonic S10, 30 W) two times for 5 min at room temperature, with pre-set power level and continuous operation at 37 kHz. The pellet and the supernatant fractions of the nanoerythrosome suspension were obtained by ultracentrifuge separation of the sonicated ghost membrane using a Beckman TL-100 ultracentrifuge with TLA 100.1 fixed angle rotor (average 96 427 × g, 30 min). The upper layer of the supernatant, expected to be rich in released membrane proteins (approx. 50 % of the total volume, denoted below as "supernatant" and abbreviated as SPROT), was removed. The sediment was resuspended in PBS buffer after the removal of the liquid phase. This fraction will be referred to as "pellet" and abbreviated as PELL in the following. The protein content of both fractions was determined by Bradford assay.

Finally, the dry LPC lipid film (made by dissolving LPC in chloroform containing 30 v/v % methanol and subsequently evaporating the solvent) was hydrated with (i) the original suspension of nanoerythrosomes (NERY), (ii) the supernatant (SPROT), and (iii) the resuspended pellet (PELL) in two- and fivefold weight to weight lipid-to-protein ratios. During this process, slight ultrasound treatment was applied to obtain homogeneous size distributions, monitored by DLS measurements.

2.3. Transmission electron microscopy combined with freeze fracture (FF-TEM)

Approximately 1 μl droplets of the samples were used for freeze fracturing. These were pipetted onto a golden sample holder and rapidly frozen in liquid freon, then put into liquid nitrogen. Fracturing was performed at −100 °C in a Balzers freeze-fracture device (Balzers BAF 400D, Balzers AG, Liechtenstein). A replica was made from the fractured surface with vaporized carbon and platinum. The replica was cleaned from the remainders of the original sample with surfactant solution and distilled water, and it was transferred to a 200-mesh copper grid for examination in a transmission electron microscope (MORGAGNI 268D, FEI, The Netherlands).

2.4. Fourier transform infrared spectroscopy (FT-IR)

ATR-FTIR spectra were acquired using a Varian 2000 FTIR Scimitar Series (Varian, Inc, USA) spectrometer equipped with a liquid nitrogen cooled mercury-cadmium telluride (MCT) detector and fitted with a 'Golden Gate' single reflection diamond ATR accessory (Specac ltd, UK). Three μl of sample was spread onto the diamond surface and a thin, almost dry but still hydrated film was obtained by slowly evaporating the solvent under ambient conditions (for approx. 5 min). Typically, 64 scans were collected at a nominal resolution of 2 cm^{-1}. After each data acquisition, ATR correction using advanced ATR correction algorithm (crystal refractive index: 2.37; sample refractive index: 1.5; crystal angle of incidence: 45°) was performed. Calculation of spectroscopic protein-to-lipid (P/L) ratio was performed on subtracted spectra, after PBS background correc-

tion. For area determination of lipid and protein bands we used the 1780–1380 cm^{-1} spectral region. The three major bands (lipid C=O at 1739 cm^{-1}; amide I around 1651 cm^{-1} and amide II at 1543 cm^{-1}) were fitted by mixed Gaussian-Lorentzian functions. For P/L calculation the area under the fitted amide I and lipid C=O bands was used. To assess protein secondary structure, the amide I band was deconvoluted by a curve fitting algorithm. Band positions for curve fitting were estimated using the second derivative of the spectrum, and band shapes were approximated by mixed Gaussian and Lorentzian functions until reaching the minimum in χ^2. The value of the Lorentzian contribution, the intensities and the bandwidth of each component were allowed to vary. After the fitting procedure, the relative contribution of a particular component was calculated from the integrated areas of the individual components. For all spectral manipulations the GRAMS/32 software package (ThermoGalactic, US) were used.

2.5. Circular dichroism (CD)

CD spectra were collected using a JASCO J-1500 spectropolarimeter at room temperature. Samples were diluted in PBS to a final protein concentration of approx. 5 mg/ml and measured in a 0.1 cm path-length cylindrical quartz cuvette (Hellma, Plainview, NY, United States) in continuous scanning mode at a rate of 50 nm/min, with a data pitch of 0.5 nm, response time of 2 s, bandwidth of 2 nm, and 3 times accumulation. All spectra were corrected by subtracting a matching blank, and smoothed.

2.6. Protein identification using tandem mass spectroscopy (MS) coupled with nano liquid chromatography (nanoLC-MS(MS)

Proteins were extracted from samples by repeated freeze–thaw cycles. Following tryptic digestion of 12 μg protein/sample, the samples were desalted using PierceTM C18 spin columns (Thermo Fisher Scientific, Waltham, MA, United States) as previously described [22]. The resulting peptides were analysed using a Dionex Ultimate 3000 RSLCnano liquid chromatograph (LC, Dionex, Sunnyvale, CA) coupled to a high-resolution Bruker Maxis II Q-TOF mass spectrometer (MS, Bruker, Bremen, Germany), equipped with a CaptiveSpray nanoBooster ionization source. The peptides were separated using gradient elution on a 25 cm Waters Peptide BEH C18 nanoACQUITY 1.7 μm particle size UPLC column (Waters, Milford, MA). Label-free protein quantitation (LFQ) was performed using MaxQuant on a focused Homo sapiens database combining Byonic (v3.5.0, Protein Metrics, Cupertino, CA) search results from all MS/MS analyses [23]. Byonic search was performed against the Swissprot Homo sapiens database [24], applying the following search parameters: trypsin enzyme, 10 ppm peptide mass tolerance, 20 ppm fragment mass tolerance, 2 missed cleavages. Carbamidomethylation was set as fixed modification, and the following modifications were included as variable modifications: oxidation (M) as common; acetylation (protein *N*-term), ammonia-loss (*N*-term C), Glu → pyro-Glu (*N*-term E) and Gln → pyro-Glu (*N*-term Q) as rare. Requirements for protein identification were the following, set in Scaffold 4.10 (Proteome Software, Portland, OR, [25]) with LFDR-rescoring on: 95 % peptide confidence threshold, minimum of two unique peptides. The protein-level False Discovery Rate was set to 1 %.

2.7. Bradford protein assay (UV–vis)

The total protein content of ghost (GHOST) and its derivatives (NERY, SPROT, PELL) was determined using the Bradford assay that involves the binding of Coomassie Brilliant Blue G-250 dye to proteins [26]. Bovine serum albumin (BioRad) was used as standard, from which eight consecutive dilution steps (0–25 μg/ml) were carried out in three parallel sequences. To 5 μl of each standard and unknown sample solution, 250 μl dye reagent was added and the mixtures were vortexed for 15 *sec*. The samples were incubated at room temperature for at least 5 min and the absorbance was measured at 595 nm with a BioTek Synergy 2 plate reader on 96 well plates.

2.8. Dynamic light scattering (DLS)

A W130i dynamic light scattering apparatus (AvidNano, United Kingdom) was used for measuring the average size and size distribution of the samples [27]. 5 μl of the samples was diluted with 75 μl PBS buffer and measured in a microcuvette. The analysis of the measurement data was performed with the i-Size software supplied with the apparatus.

2.9. Small-angle X-ray scattering (SAXS)

Small-angle X-ray scattering measurements were performed at the Austrian SAXS beamline of the Elettra synchrotron (Trieste, Italy) [28]. The samples were filled into the same quartz capillary of 1.5 mm nominal outer diameter, washed thoroughly first with water then ethanol between measurements of different samples. After proper sealing, this was placed in a temperature-controlled metal block, which was inserted into the air gap of the beam path, enclosed by two Mylar® foils. Measurements were done using monochromatized and collimated radiation of 8 keV photon energy. The scattering pattern was recorded in the range of 0.5 – 5 nm^{-1} in terms of the scattering variable, q (defined as $q = \frac{4\pi}{\lambda} \sin\theta$, where 2θ is the scattering angle and λ is the X-ray wavelength), using a Pilatus 1 M two-dimensional positive sensitive CMOS hybrid pixel detector (Dectris ltd, Baden, Switzerland). In order to be able to assess sample stability during the experiment, twenty exposures, each 1 s long, were made for each sample, including the relevant aqueous buffers. The individual exposures were corrected for beam flux, geometric effects, and instrumental background. The corrected scattering patterns were azimuthally averaged to yield one-dimensional scattering curves for each sample.

3. Results and discussion

3.1. Characterization of the ghost and ghost-derived nanoerythrosomes with freeze-fracture transmission electron-microscopy

The unique combination of the freeze-fracture (FF) procedure with transmission electron microscopy (TEM) provides means for the observation of the surface morphology of haemoglobin-free ghosts (GHOST) and their derivatives: nanoerythrosomes (NERY) that are obtained from ghosts by ultrasonication, and the two characteristic fractions produced by ultracentrifugation of NERY: the supernatant rich in released membrane proteins (SPROT) and the pellet (PELL) containing most of the lipids. FF-TEM images shown in panel I of Fig. 1 attests the GHOST being composed of large, laterally extended (about 2–4 μm) sheets or frequently giant, unilamellar-like vesicles. A closer look shows the membrane proteins decorating the surface of the ghosts as closely packed grains typically smaller than 10 nm. The usually convex inner half of the bilayer (the so-called "P" surface, *cf* inset A of Fig. 1) contains more, while the concave, outer half (the "E" surface, inset B) contains less of these particles, in line with our previous FF-TEM results [15].

Ultrasonic treatment induces a significant change in morphology, as instead of heterodisperse large sheets, stable (-45 mV ζ-potential), nearly spherical, small nanoerythrosomes are formed

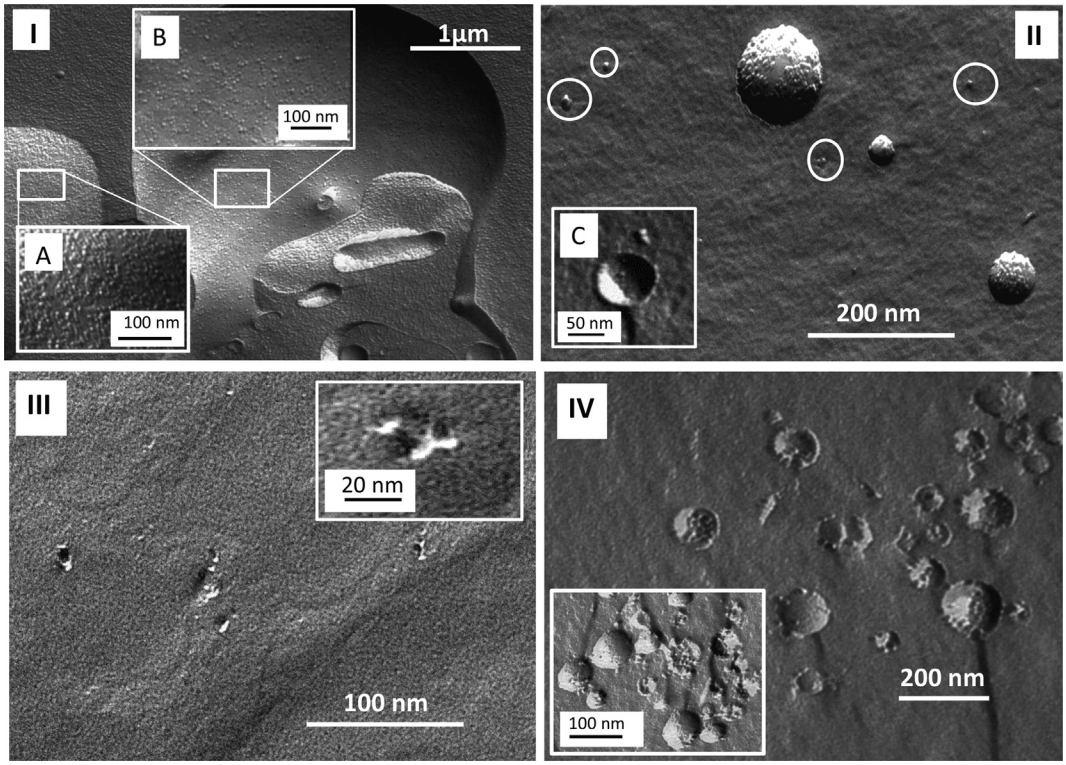

Fig. 1. Freeze-fractured surface morphology of erythrocyte ghosts (GHOST, panel I); nanoerythrosomes formed during ultra-sonication of ghosts (NERY, panel II), released membrane-proteins in the supernatant of ultracentrifuged nanoerythrosomes (SPROT, panel III) and pellet of ultracentrifuged nanoerythrosomes (PELL, panel IV).

with an average diameter of 155 nm shown in panel II of Fig. 1. The surface features of the NERY are markedly different from GHOST. Their outer surfaces are densely and heterogeneously packed with proteins and protein aggregates. Some entirely broken through NERYs also appear, showing that the inner surfaces are less covered by proteins (inset C in panel II of Fig. 1). Apart from these, many small (10 – 30 nm) entities are also visible in the medium (marked by circles in panel II of Fig. 1). These particles are presumably solubilized membrane proteins or protein aggregates with their lipid surroundings, released from the GHOSTs during ultrasound treatment. It cannot be precluded, that free proteins were already present in the precursor ghost system, but their occurrence was not observed on the micrographs. Panel III of Fig. 1 shows the released proteins of the supernatant of centrifuged nanoerythrosomes (SPROT) as small particles and aggregates under higher magnification (inset in panel III of Fig. 1). Their size is heterogeneous, falling in the range between 10 and 30 nm. Dynamic light scattering gives a characteristic mean diameter of approx. 25 nm (with the assumption that the particles are spherical). The pellet fraction of the centrifuged nanoerythrosomes (PELL) contains rather closed entities, assumably more or less destroyed nanoerythrosomes with protein aggregates (see panel IV of Fig. 1).

3.2. Compositional and structural studies with mass, circular dichroism and infrared spectroscopy

Proteomic analysis was carried out to detect differences in the protein pattern of the membrane-associated samples (GHOST, NERY, PELL) and the released proteins (SPROT). Despite the detailed, recently published proteomic data [29,30], a fresh study was necessary to obtain information about these fractions. In total 166 proteins were identified with mass spectrometry in the four samples. 121, 123, 137 and 80 different proteins were found in GHOST, NERY, PELL and SPROT samples, respectively, of which 63 were present in all four (although undoubtedly, the preparation method might bear influence on the actual protein composition of the fractions). The four most frequent proteins were the same in each fraction: the membrane skeleton proteins ankyrin and spectrin (both α and β chains of the latter), as well as the integral membrane protein Band 3. [31–36]. To give a semi-quantitative description, a label-free quantitation (LFQ) was carried out using MaxQuant. MaxQuant LFQ values of a given protein in a given sample were normalized to the total LFQ intensity of the respective sample. Therefore the vertical axis contains the relative abundance of a given protein to the relative abundance of all proteins in the given sample shown in Fig. 2. It is obvious that spectrin α is increased, while the Band 3 membrane protein decreased significantly in SPROT. The changes for the skeletal and membrane components are opposite in the PELL sample. Different number of proteins were found to be exclusive for each fractions, shown by the Venn diagram also in Fig. 2. The relatively small number of exclusive proteins in SPROT (compared to PELL) indicates that a moderate sonication process may cause a non-specific release of membrane-associated proteins.

To assess changes in protein structure, circular dichroism (CD), and ATR Fourier-transform infrared (FT-IR) spectroscopy was applied. The former is the standard method for solution phase samples even in membrane environment, while the latter is an excellent tool to follow even subtle conformational variations upon minor perturbations detected in dry film samples.

Far-UV CD spectra (Fig. 3) of the fractions containing lipid bilayers, i.e., GHOST, nanoerythrosomes (NERY), and the pellet (PELL), displayed similar spectral shapes with minima at $\sim$ 210 nm and $\sim$ 223 nm. For the supernatant fraction of centrifuged NERY (SPROT), the corresponding peaks are blue shifted to 208 and 222 nm. Both spectral patterns are compatible with a mainly helical character of the major protein components identified, in the individual fractions i.e.spectrins, ankyrin, and Band 3. CD spectra

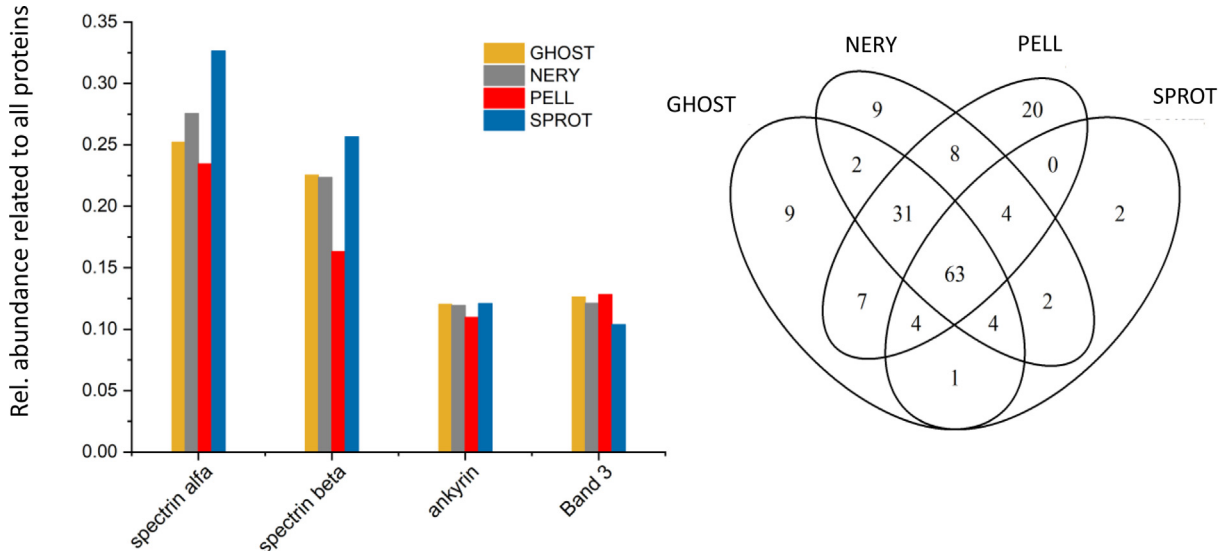

Fig. 2. Changes in ratio of characteristic four skeletal and membrane proteins in the four (GHOST, NERY, SPROT and PELL) samples (left). The number of exclusive and common proteins are shown in Venn diagram (right).

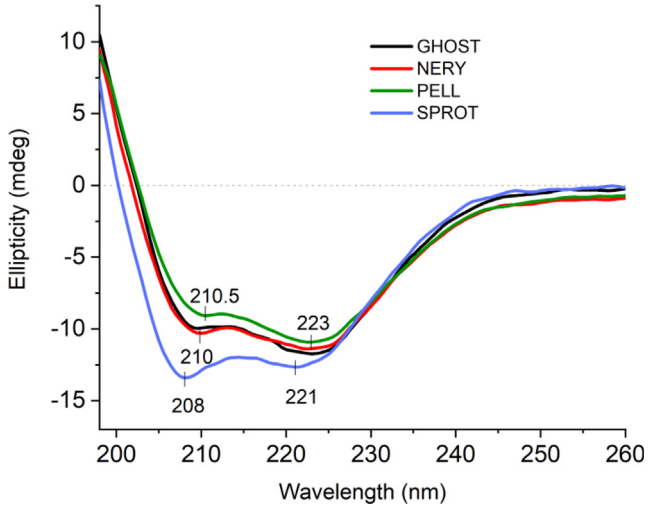

Fig. 3. CD spectra of ghost (GHOST) and its derivatives: nanoerythrosomes (NERY), pellet (PELL) and supernatant (SPROT).

of soluble helical proteins are characterized by minima at 208 nm and 222 nm, closer to the values found for SPROT. Accordingly, the SPROT fraction may contain proteins resembling rather solubilized proteins. Definite differences were also observed in the relative intensity of the two minima, which can report on the associated state of the helices, particularly for spectrin chains [37,38]. The ratio I_{222}/I_{208} less than 1 for the SPROT fraction could be indicative of re-arranged helices of looser contacts compared to their state in GHOST. Alternatively, spectral variations might indicate partial denaturation of the proteins upon the sonication process, resulting in no complete unfolding but in native-like, presumably molten globule states, where most of the secondary structural elements are maintened but re-arranged. Indeed, spectral changes similar to that detected here were reported for both helical and sheet-rich proteins upon transition to molten globules [39,40]. Molten globules are known to be enriched in exposed hydrophobic patches, thus being prone to aggregation.

The partial protein solubilisation process upon formation of NERY particles from GHOST where membrane-associated proteins, along with a reduced lipid content, are separated from the ghost membrane matrix including membrane skeleton, the re-arrangement of their structures and contacts can finally lead to the formation of the protein-rich particles observed in TEM micrographs.

The increase in relative protein content of the supernatant fraction is further confirmed by FT-IR spectra. Bands with the highest intensities from the spectra of ghost membrane and its derivatives can be assigned to functional groups in either the lipids or the proteins (Fig. 4) [41]. The characteristic lipid group frequencies appear at wavenumbers approximately 2800–3300 cm^{-1} for C—H and 1700–1800 cm^{-1} for C═O stretching vibrations [42,43], while proteins exhibit the amide I (1600–1700 cm^{-1}) and amide II (1500–1600 cm^{-1}) bands of peptide bonds [44]. Changes in the secondary structure and molecular environment of the proteins manifest themselves in changes to the shape and position of the amide bands.

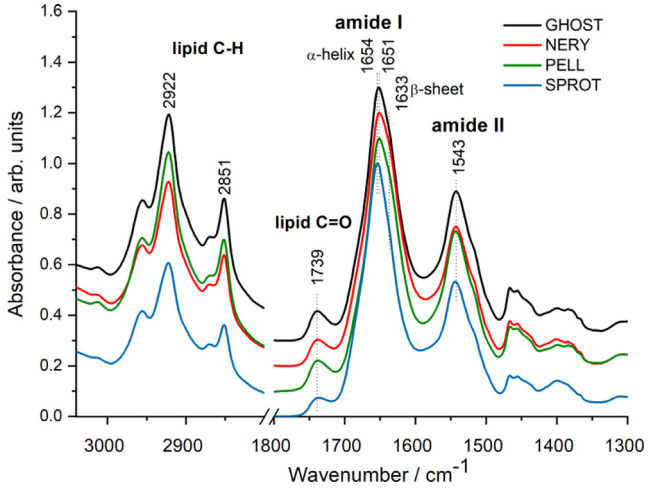

Fig. 4. Amide I and II bands and C—H stretching vibration regions from FT-IR spectra of ghost (GHOST), nanoerythrosomes (NERY), pellet (PELL) and supernatant (SPROT). Spectra are normalized to the amide I intensity and shifted vertically for better visualization.

By deconvolution of the amide I region of the spectra (1600–1700 cm^{-1}), the component bands corresponding to α–helix (around 1653 cm^{-1}), β–sheet (1633 cm^{-1}), turn (1681 cm^{-1}) and intermolecular β-sheet (1617 cm^{-1}) secondary structures can be determined (Table 1). By CD spectroscopy it was seen that the α-helical structure dominates in every fraction. Indeed, the analysis of amide I band components confirms the prevalent contribution of the helical component. (Supplementary Material 1.).

The spectroscopic α-helix/β-sheet ratio is nearly 2.5 – 2.9, with a slight deviation in the case of the NERY and the PELL fraction. A difference could be identified in the case of SPROT, where the β-sheet content seemed to be significantly less (spectroscopic α-helix/β-sheet ratio in this case is 3.6).

Furthermore, the C—H (at 2922 and 2851 cm^{-1}) and the C═O (at 1739 cm^{-1}) stretching vibrations of the lipid acyl chains and of the glycerol backbone, respectively, are significantly suppressed in the supernatant fraction. Since the C═O stretching band (νC═O) of the lipids and the amide I band of the proteins are well separated, it is possible to calculate a so-called spectroscopic protein to lipid ratio (P/L) [16,41]. For this purpose, the ratio of the integrated intensities of the two bands are used. The estimated spectroscopic P/L values are shown in Table 1. Although admittedly not the same as the stoichiometric ratios, these do express the enrichment or loss in protein content. This is in line with the presence of protein-rich particles formed from released membrane proteins in SPROT, as previously assumed from TEM and CD results. Moreover, the peak of amide I band envelope is shifted (from 1651 to 1654 cm^{-1}), suggesting an altered helix environment. This observation and the increase in the amide I/amide II intensity ratio, the latter related to changes in the tertiary structure of proteins, is consistent with the hypothesis of the formation of molten globules deduced from CD signal of SPROT.

3.3. Nanostructure of the mixture of ghost derived systems and lysophospholipids

The addition of lysophospholipid to the separated ghost derivates (NERY, PELL and SPROT) results in the nanoparticle formation. Experience shows that ultrasonication is hardly required in the presence of LPC: at higher lysophospholipid ratio the spontaneous formation of nanoparticles is rapid, and the cloudy, turbid mixture of precursors and LPC turns into a clear, transparent liquid, indicating the significant decrease in particle size.

The SAXS curves of the three sonicated systems (NERY, PELL and SPROT) with 2:1 and 5:1 LPC/protein weight to weight ratios are shown in Fig. 5. After a monotonic decrease at the small-q region of the scattering patterns, a wide hump appears at intermediate values of the scattering variable (from 0.8 to 2 nm^{-1}), which is more expressed at higher LPC ratios. Both features are characteristic for micelle-like scatterers: the small-q part carrying information on the overall size of the particles, while the hump describes the internal structure. Additionally, the SPROT-LPC systems exhibit an upturn of the curve in the small-q range, which can be ascribed to other, larger scattering objects. The reason can be the simultaneous presence of protein aggregates and lipid nanoparticles, especially in the case of the system with 2 LPC to protein ratio. Considering the above-described properties, the SAXS curves can be classified into three, rather than two shape categories, suggesting that the precursor system has a stronger influence than the added LPC.

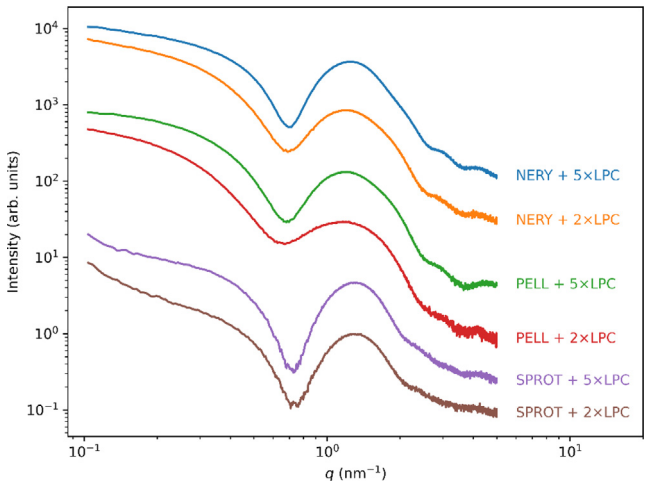

Fig. 5. One-dimensional SAXS patterns of the NERY, PELL and SPROT nanoerythrosome fractions with two- and fivefold lysophospholipid to protein ratios. The curves are shifted vertically for better observability.

As already said, small-q scattering is traditionally associated with the overall size of the nanoparticles, or small unilamellar vesicles, too [45]. The relationship is not straightforward, however, where the scattering particle contains domains with both positive and negative electron density contrast relative to the level of the aqueous solvent (e.g., chain and head region of lipids, proteins). For these, the Guinier radius, even if it can be derived at all, may not be indicative of the geometric size of the particles. Presumably, our nanoparticles are such micelle-like mixtures, but since their central part does not consist solely of the hydrocarbon chains of the lipids, the term "micelle" would be a misnomer. Nevertheless, structural models usually applied for micellar systems can be useful in this case, too.

3.4. Structural model of the nanoerythrosomes(NERY)-LPC mixtures

To obtain more detailed insight into the structural variations upon the addition of LPC to the nanoerythrosomes (NERY), the SAXS data were fitted by core–shell ellipsoid of revolution models (details for SAXS model are in Supplementary Material 2, 2.2). The fitting procedure was conducted in SasView 5.0.4 [46], using a least square algorithm, by both built-in and self-developed models written in Python. Since the optimization was performed on a relative intensity scale, and it is known that the electron density of the carbon chains is smaller than that of water, we have fixed the scattering length density of the core ($\Delta\rho_{core}$) to −1 [electron/Å^3]. The fitted parameters were the equatorial radius of core (R_{core}, the anisotropy of the core ellipsoid expressed by its aspect ratio (ε_{core} being the ratio of the lengths of the half axis of revolution and the equatorial axes), the thickness (T_{shell}) and the relative scattering length density of the shell ($\Delta\rho_{shell}$). Furthermore, a global scaling factor for

Table 1
Result of the curve fitting analysis of amide I bands assessing protein secondary structure and the spectroscopic protein-to-lipid ratios.

Sample	turn	α-helix	β-sheet	intermolec. β-sheet	P/L
GHOST	10.10 ± 0.42	57.29 ± 0.16	22.19 ± 0.72	10.41 ± 0.14	23.8 ± 3.6
NERY	9.84 ± 0.19	58.68 ± 0.61	19.92 ± 0.38	11.56 ± 0.04	23.5 ± 3.5
PELL	8.58 ± 0.11	58.17 ± 0.12	21.02 ± 0.21	12.24 ± 0.32	15.2 ± 2.7
SPROT	10.79 ± 0.40	66.57 ± 0.21	17.34 ± 0.63	5.23 ± 0.04	33.2 ± 3.9

accounting for the relative intensity scale, and an additive constant for mitigating artifacts from incomplete background subtraction have been also fitted. In the case of the nanoerythrosome sample with 5 × LPC, a hard sphere structure factor also had to be included to fit the data, resulting in two additional parameters: a hard sphere radius (R_{HS}) and the volume fraction (η). The structure factor was implemented using the decoupling approximation. The shape of particles with their equatorial electron density profiles are shown in upper part of Fig. 6. The fitted scattering curves are plotted in the Supplementary Material 2.1, while the fitted parameters of the core–shell models are summarized in Table 2.

The equatorial core radius and shell thickness of the NERY-based particles stay practically constant with increasing LPC (R_{core} = 1.03 nm and 1.04 nm, T_{shell} = 2.8 nm and 2.7 nm for 2 × and 5 × LPC, respectively), however the anisometry of the 5 × LPC system is lower (ε_{core} = 3.1 instead of 4.7), suggesting that the particles are less elongated. This trend can be the consequence of the lipid content of the nanoerythrosomes. Namely, the membrane lipids have an effective cylindrical shape, preferring the formation of flat layers. Thus, the addition of the conical-shaped LPC increases the curvature in the entire interface of the assembly.

3.5. Structural modelling of the pellet(PELL)-LPC mixtures

The above introduced core–shell ellipsoid of revolution model was not enough to describe the scattering curve of the PELL-LPC mixtures (Supplementary Material 2.2). In the case where 2 × LPC was added to the pellet fraction, an extended model with a hydrophobic core, a hydrophilic shell (T_{shell1}) and an additional, moderately hydrophilic second shell (T_{shell2}) was required, as shown in the bottom part of Fig. 6. The second shell increased the extension of the lipid nanoparticle; however, its low scattering contrast indicates the high hydration of the surface, presumably being a protein corona. The other feature, namely the increase in the local minimum between 0.6 and 0.7 nm^{-1} on the scattering curve of this sample, (*cf.* Fig. 5) can be attributed to a "baseline" scattering of proteins not integrated into the nanoparticles. This effect has been accounted for with a Gaussian chain intensity component (detailed in the Supplementary Material), resulting in two more fit parameters, the radius of gyration of the proteins ($R_{g,protein}$) and a relative intensity scaling factor. This contribution was not required with the 5 × LPC sample, probably because all proteins have been accommodated by the increased amount of LPS. Interestingly, the PELL + 5 × LPC resembles more the

Table 2
Structural parameters of the ellipsoidal model for the lipid nanoparticles having the mixture of nanoerythrosomes and lysophospholipids.

	NERY + 2 × LPC	NERY + 5 × LPC
$\Delta\rho_{core}$	−1 (fixed)	−1 (fixed)
R_{core}[nm]	1.027 ± 0.004	1.036 ± 0.0015
ε_{core}	4.65 ± 0.03	3.10 ± 0.01
T_{shell}[nm]	2.767 ± 0.005	2.712 ± 0.002
$\Delta\rho_{shell}$	0.157 ± 1.6 × 10^{-4}	0.116 ± 5.3 × 10^{-5}
R_{HS}[nm]	–	3.75
η	–	0.0906 ± 6.6 × 10^{-4}

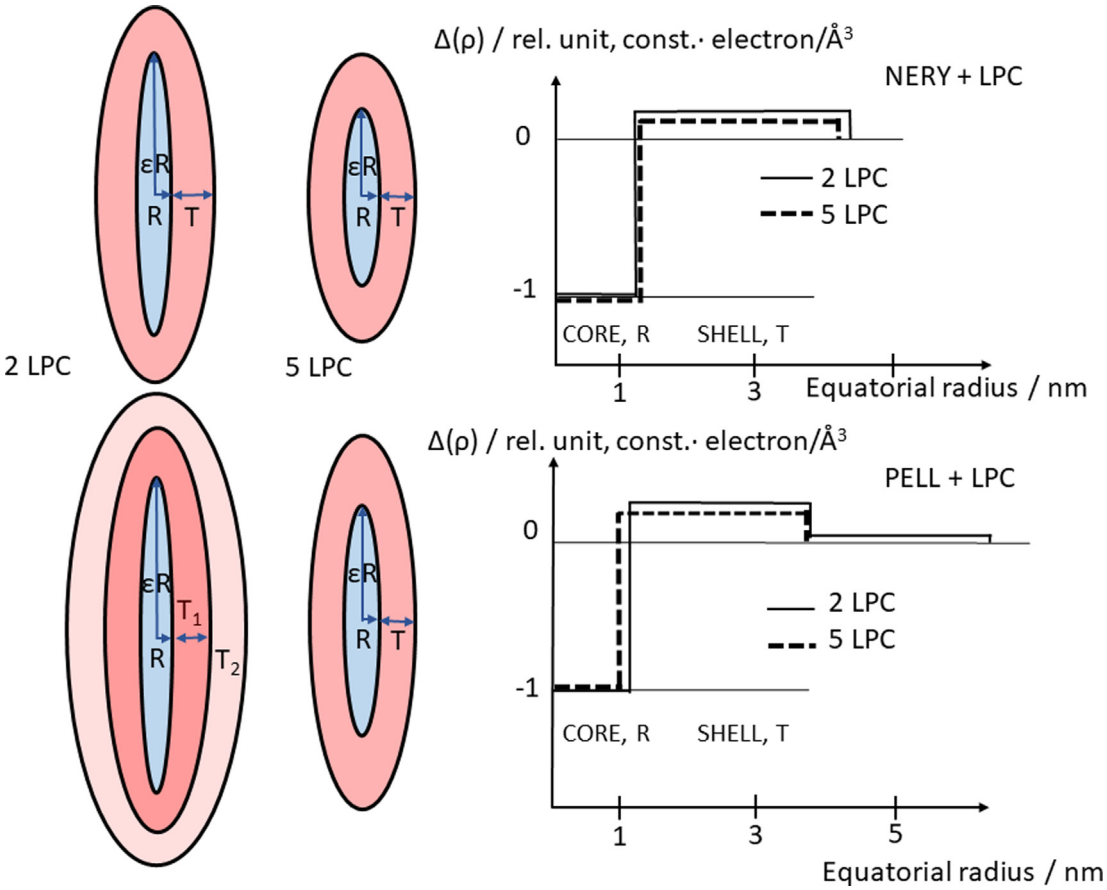

Fig. 6. Ellipsoid models (left) of nanoparticles obtained by addition of lysophospholipid (LPC) to nanoerythrosomes (NERY, top) and their ultracentrifuge pellet (PELL, bottom), and their fitted equatorial scattering length densities ($\Delta\rho$, right). The hydrophobic and hydrophilic shells are demonstrated with different colours in the model sketch (hydrophobic core region: blue; hydrophilic shells: pink). (For interpretation of the references to colour in this figure legend, the reader is referred to the web version of this article.)

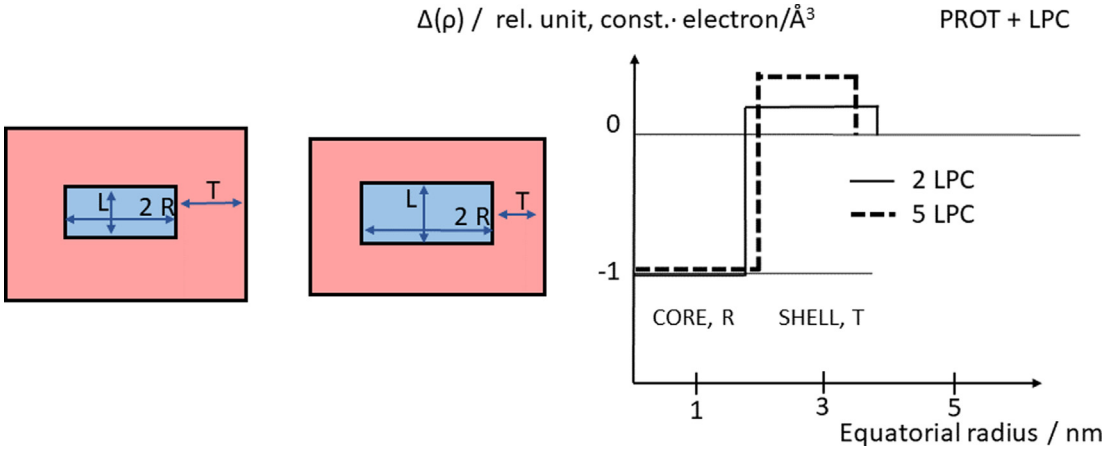

Fig. 7. The cylinder models (left) of nanoparticles consisting of released membrane proteins in the supernatant (SPROT) and lysophospholid (LPC), and their fitted equatorial scattering length densities ($\Delta\rho$, right). The hydrophobic and hydrophilic regions are demonstrated with different colours in the model sketch (hydrophobic region: blue; hydrophilic region: pink). (For interpretation of the references to colour in this figure legend, the reader is referred to the web version of this article.)

Table 3
Structural parameters of the ellipsoidal model for the lipid nanoparticles having the mixture of pellet and lysophospholipids.

	PELL + 2xLPC	PELL + 5xLPC
R_{core}[nm]	1.234 ± 0.028	1.055 ± 0.003
ε_{core}	6.38 ± 0.16	4.07 ± 0.02
T_{shell1}[nm]	2.59 ± 0.04	2.74 ± 0.01
$\Delta\rho_{shell1}$(relative to $\Delta\rho_{core}$)	0.224 ± 0.016	0.137 ± 0.001
T_{shell2}[nm]	2.63 ± 0.04	
$\Delta\rho_{shell2}$(relative to $\Delta\rho_{core}$)	0.022 ± 0.001	
$R_{g.protein}$[nm]	2.18 ± 0.61	
σ_{core}[nm]	0.2 (fixed)	0.2 (fixed)
σ_{shell}[nm]	0.2 (fixed)	0.2 (fixed)

NERY + LPC samples. To increase the quality of the fit, the electron density profiles were convoluted by Gaussian curves (width characterized by σ_{in} and σ_{out}) to make the shell-solvent interfaces smooth [47]. The convolution width parameters were fixed at 0.2 nm in a "trial and error" manner. Supposedly the increased LPC ratio contributed to the embedding of proteins into the outer region, whereby the second shell ceased to exist, but the interfaces between core and shell and shell and solvent are rather smooth than sharp. The fitted parameters are summarized in Table 3. The models are described in detail in the Supplementary Material 2.2 and the fitted curves are plotted in Supplementary Material 2.3.

Of the two PELL + LPC samples, the 5 × LPC one has smaller core radius (1.05 nm compared to 1.23 nm), while the ellipticity of the core decreases from 6.4 to 4.1 when more lipid is added. The volume of 2 × LPC particle is approximately 7200 nm^3. The total radius of the core of 5 × LPC, including the smearing is $R_{coretotal} = R_{core} + 2\sigma_{core}$ and the total thickness of the shell is $T_{shelltotal} = T_{shell} + 4\sigma_{shell}$. This means that PELL + 5LPC particle has 1.5 nm core radius and 3.2 nm shell thickness. The volume is 1800 nm^3 for PELL + 5LPC particle. Such a large deviation in the volume of the two systems can be explained by the presence or absence of the third region. Although a second shell was needed in the case of PELL + 2LPC for a good fit of the measured data, its electron density contrast is only slightly larger than the solvent level, possibly causing the overestimation of the volume by incorporating the well-hydrated, fuzzy surface of the particles.

Interestingly, the samples derived from NERY and PELL all had high aspect ratios, showing elongated ellipsoids, induced by self-assembly of a mixture of cylindrical natural lipids and strongly conical lyso-phospholipids.

3.6. Structural modeling of the supernatant(SPROT) + LPC systems

Before the LPC is added, the SAXS curve of the SPROT fraction has two turns in the beginning and the final sections, indicating the existence of two, well-separated size ranges, with their average diameters falling into the range of approximately 1 and 30 nm (*cf.* Supplementary Material 4). Possibly these correspond to the proteins decorating the outer surface of nanoerythrosomes (10 nm) and to the released proteins (10 – 30 nm) observed by FF-TEM (II and III panels of Fig. 1). The small particles (in approx. 1 nm size range) represent the small proteins, which are also present in the released membrane proteins. The scattering curves of SPROT + LPC samples were fitted by the built-in core–shell cylinder model of SasView, and the parameters are summarized in Table 4 and the models are shown in Fig. 7. (The experimental and fitted SAXS curves are presented in Supplementary Material 2.5).

The fitted parameters were the radius (R_{CS} = 1.8 and 2.1 nm for the sample with 2 × LPC and 5 × LPC, respectively) and the length of the core cylinder (L_{core} = 1.46 and 2.11 nm), and the thickness and the scattering length density of the shell (T_{shell} = 2.05 and 1.53 nm, $\Delta\rho_{shell}$= 0.158 and 0.332 for 2 × LPC and 5 × LPC systems, respectively). Upon increasing the amount of the added LPC, the cross-section radius and length of the cylinder increases, while the thickness of the shell decreases. The volume of a cylinder is $V_{cylinder} = (R_{CS} + T_{shell})^2\pi(2T_{shell} + L_{core})$. For SPROT + 2 × LPC this is ~ 260 nm^3, while for 5 × LPC ~ 210 nm^3.

In summary, in all cases the volume of the particles decreased by increasing the amount of added LPC. This behaviour is somewhat expected, since surface formation is energetically preferred on the addition of amphiphilic molecules, as this way the overall free enthalpy of the system decreases. Thus, smaller particles are formed in order to obtain a larger total surface area.

Table 4
Structural parameters of the cylinder model for the lipid nanoparticles prepared from SPROT + LPC.

	SPROT + 2 × LPC	SPROT + 5 × LPC
R_{CS}[nm]	1.79 ± 0.03	2.08 ± 0.01
L_{core}[nm]	1.46 ± 0.04	2.12 ± 0.02
T_{shell}[nm]	2.04 ± 0.04	1.53 ± 0.02
$\Delta\rho_{shell}$(relative to $\Delta\rho_{core}$)	0.158 ± 0.001	0.333 ± 0.008

4. Conclusion

Although the nanoerythrosomes (NERY), and its two main ultracentrifugation fractions, the pellet (PELL) and supernatant (SPROT) exhibit nearly the same protein patterns, their original lipid contents are different. The lipids in NERY are membrane lipids: typical "bilayer"-preferring, cylinder-shaped ones, favouring the formation of vesicle-like objects. The addition of curvature-inducing, inversely conical lysophosphocholine (LPC) molecules results in the formation of prolate objects, as found by small-angle X-ray scattering, based on a core–shell model approximation. Within the frame of this model, the shape of the objects becomes less anisotropic (more spherical) with increasing LPC ratio, and the curvatures extend on the entire surface of the nano-ellipsoids, as the consequence of the lipid packing. In case of the PELL samples, having the highest membrane lipid-to-LPC ratio, the simple "two-phase" core–shell ellipsoidal model needs to be improved by either accounting for the smoothness of the core–shell and shell-solvent interfaces or introducing an additional shell or a Gaussian chain contribution. This indicates that for smaller amount of additional LPC, the resulting nanoparticles have a more complex shell structure, with a significant part of the released membrane proteins still free in the aqueous phase. If more of the same lipid is added, these lipid molecules become dominant over the membrane-originated, bilayer-preferring lipids, resulting in a more regular "two-phase" structure, simultaneously incorporating most of the proteins.

As it was concluded by IR measurements, the SPROT fraction carries only a relatively small amount of membrane lipids. The lack of these causes significantly different self-assembly of LPC and protein molecules, reflected in the different shape of the produced nanoparticles. The experimental data is adequately described by a cylindrical two-phase core–shell structural model, because the geometrical shape of these nanoparticles built from the released membrane proteins is expected to be rather a flat, disk-like cylinder than ellipsoid. Presumably, the proteins with a given lipid represent a less complex system, where the characteristic interdigitated packing of LPC is accentuated as the length of the hydrocarbon core represents only one single hydrocarbon chain-length (1.5 and 2.1 nm). The high ratio of LPC also manifests in the mixtures of other ghost-derived fractions (NERY, PELL), where the diameter of the cores ($2R_{core}$) also do not extend to twice the typical length of the lipid chains. It seems that erythrocyte ghost and its derivatives offer a biologically relevant platform for further nanoparticle tailoring, even allowing the addition of further artificial (pharmaceutical) proteins.

Data availability

Data will be made available on request.

Declaration of Competing Interest

The authors declare that they have no known competing financial interests or personal relationships that could have appeared to influence the work reported in this paper.

Acknowledgements

The authors are indebted to Ms Teréz Kiss for the FF-TEM experiments. The project was supported by the National Research, Development and Innovation Office of Hungary under grants K131657 (A. Bóta) and K131594 (J. Mihály) and also by the Project no. 2018-1.2.1-NKP-2018-00005 under the 2018-1.2.1-NKP funding scheme (A. Bóta, Z. Varga). The Protein research program of the Hungarian Academy of Sciences (MEDinPROT, A. Bóta) is acknowledged. A. Bóta thanks the SAXS beamtime at ELETTRA (Trieste, Italy) in the frame of CERIC-ERIC research panel (proposal id 20192058, 20212158). A. Wacha and Z. Varga were supported by the János Bolyai Research Scholarship of the Hungarian Academy of Sciences.

Appendix A. Supplementary material

Supplementary data to this article can be found online at https://doi.org/10.1016/j.molliq.2022.120791.

References

[1] G. Gregoriadis, Liposomes and MRNA: two technologies together create a COVID-19 Vaccine, Med. Drug Discovery 12 (2021), https://doi.org/10.1016/j.medidd.2021.100104.
[2] J.A. Loureiro, B. Gomes, M.A. Coelho, M. Carmo Pereira, M. do, S. Rocha, Targeting nanoparticles across the blood-brain barrier with monoclonal antibodies, Nanomedicine 9 (2014) 709–722, https://doi.org/10.2217/nnm.14.27.
[3] S. Ramishetti, R. Kedmi, M. Goldsmith, F. Leonard, A.G. Sprague, B. Godin, M. Gozin, P.R. Cullis, D.M. Dykxhoorn, D. Peer, Systemic Gene Silencing in Primary T Lymphocytes Using Targeted Lipid Nanoparticles, ACS Nano 9 (2015) 6706–6716, https://doi.org/10.1021/acsnano.5b02796.
[4] M.L. Guevara, F. Persano, S. Persano, Advances in lipid nanoparticles for MRNA-based cancer immunotherapy, Front. Chem. 8 (2020) 963, https://doi.org/10.3389/fchem.2020.589959.
[5] J. Fang, H. Nakamura, H. Maeda, The EPR effect: unique features of tumor blood vessels for drug delivery, factors involved, and limitations and augmentation of the effect, Adv. Drug Deliv. Rev. 63 (2011) 136–151, https://doi.org/10.1016/j.addr.2010.04.009.
[6] H. Maeda, J. Wu, T. Sawa, Y. Matsumura, K. Hori, Tumor Vascular Permeability and the EPR Effect in Macromolecular Therapeutics: a Review, J. Control. Release 65 (2000) 271–284, https://doi.org/10.1016/s0168-3659(99)00248-5.
[7] H. Zhang, Erythrocytes in Nanomedicine: an optimal blend of natural and synthetic materials, Biomater. Sci. 4 (2016) 1024–1031, https://doi.org/10.1039/C6BM00072J.
[8] A. Lejeune, M. Moorjani, C. Gicquaud, J. Lacroix, P. Poyet, R. Gaudreault, Nanoerythrosome, a new derivative of erythrocyte ghost: preparation and antineoplastic potential as drug carrier for daunorubicin, Anticancer Res. 14 (1994) 915–919.
[9] Y.-C. Kuo, H.-C. Wu, D. Hoang, W.E. Bentley, W.D. D'Souza, S.R. Raghavan, Colloidal Properties of Nanoerythrosomes Derived from Bovine Red Blood Cells, Langmuir 32 (2016) 171–179, https://doi.org/10.1021/acs.langmuir.5b03014.
[10] S. Krishnamurthy, M.K. Gnanasammandhan, C. Xie, K. Huang, M.Y. Cui, J.M. Chan, Monocyte cell membrane-derived nanoghosts for targeted cancer therapy, Nanoscale 8 (13) (2016) 6981–6985.
[11] T. Liu, C. Shi, L. Duan, Z. Zhang, L. Luo, S. Goel, W. Cai, T. Chen, A Highly hemocompatible erythrocyte membrane-coated ultrasmall selenium nanosystem for simultaneous cancer radiosensitization and precise antiangiogenesis, J. Mater. Chem. B 6 (2018) 4756–4764, https://doi.org/10.1039/C8TB01398E.
[12] J. Su, G. Liu, Y. Lian, Z. Kamal, X. Que, Y. Qiu, M. Qiu, Preparation and characterization of erythrocyte membrane cloaked PLGA/Arsenic Trioxide Nanoparticles and Evaluation of Their in Vitro Anti-Tumor Effect, RSC Adv. 8 (2018) 20068–20076, https://doi.org/10.1039/C8RA01417E.
[13] M. Fornasier, A. Porcheddu, A. Casu, S.R. Raghavan, P. Jönsson, K. Schillén, S. Murgia, Surface-modified nanoerythrosomes for potential optical imaging diagnostics, J. Colloid Interface Sci. 582 (2021) 246–253, https://doi.org/10.1016/j.jcis.2020.08.032.
[14] X. Dong, Y. Niu, Y. Ding, Y. Wang, J. Zhao, W. Leng, L. Qin, Formulation and drug loading features of nano-erythrocytes, Nanoscale Res. Lett. 12 (2017) 202, https://doi.org/10.1186/s11671-017-1980-5.
[15] R. Deák, J. Mihály, I.C. Szigyártó, A. Wacha, G. Lelkes, A. Bóta, Physicochemical characterization of artificial nanoerythrosomes derived from erythrocyte ghost membranes, Colloids Surf., B 135 (2015) 225–234, https://doi.org/10.1016/j.colsurfb.2015.07.066.
[16] R. Deák, J. Mihály, I.C. Szigyártó, T. Beke-Somfai, L. Turiák, L. Drahos, A. Wacha, A. Bóta, Z. Varga, Nanoerythrosomes tailoring: lipid induced protein scaffolding in ghost membrane derived vesicles, Mater. Sci. Eng., C 109 (2020), https://doi.org/10.1016/j.msec.2019.110428.
[17] S.T. Tan, T. Ramesh, X.R. Toh, L.N. Nguyen, Emerging Roles of Lysophospholipids in Health and Disease, Prog. Lipid. Res. 80 (2020), https://doi.org/10.1016/j.plipres.2020.101068.
[18] N.I. Hollie, J.G. Cash, M.A. Matlib, M. Wortman, J.E. Basford, W. Abplanalp, D.Y. Hui, Micromolar Changes in Lysophosphatidylcholine Concentration Cause Minor Effects on Mitochondrial Permeability but Major Alterations in Function. *Biochimica et Biophysica Acta (BBA) - Molecular and Cell Biology of*, Lipids 1841 (2014) 888–895, https://doi.org/10.1016/j.bbalip.2013.11.013.

[19] D. Dabral, J.R. Coorssen, Arachidonic acid and lysophosphatidylcholine inhibit multiple late steps of regulated exocytosis, Biochem. Biophys. Res. Commun. 515 (2019) 261–267, https://doi.org/10.1016/j.bbrc.2019.05.106.
[20] C.A. McMullen, V. Natarajan, S.S. Smyth, Lysophospholipids and their receptors: new data and new insights into their function, Biochimica et Biophysica Acta (BBA) - Molecular and Cell Biol. Lipids 1865 (7) (2020) 158697.
[21] Z. Varga, B. Fehér, D. Kitka, A. Wacha, A. Bóta, S. Berényi, V. Pipich, J.-L. Fraikin, Size measurement of extracellular vesicles and synthetic liposomes: the impact of the hydration shell and the protein corona, Colloids Surf. BBiointerfaces 192 (2020), https://doi.org/10.1016/j.colsurfb.2020.111053.
[22] L. Turiák, P. Misják, T.G. Szabó, B. Aradi, K. Pálóczi, O. Ozohanics, L. Drahos, Á. Kittel, A. Falus, E.I. Buzás, K. Vékey, Proteomic Characterization of Thymocyte-Derived Microvesicles and Apoptotic Bodies in BALB/c Mice, J. Proteomics 74 (10) (2011) 2025–2033.
[23] J. Cox, M. Mann, Maxquant enables high peptide identification rates, individualized p.p.b.-range mass accuracies and proteome-wide protein quantification, Nat. Biotechnol. 26 (2008) 1367–1372, https://doi.org/10.1038/nbt.1511.
[24] Homo Sapiens | SWISS-MODEL Repository Available online: https://swissmodel.expasy.org/repository/species/9606 (accessed on 21 December 2021).
[25] Proteome Software Available online: https://www.proteomesoftware.com/ (accessed on 21 December 2021).
[26] M.M. Bradford, A rapid and sensitive method for the quantitation of microgram quantities of protein utilizing the principle of protein-dye binding, Anal. Biochem. 72 (1976) 248–254, https://doi.org/10.1006/abio.1976.9999.
[27] Dynamic Light Scattering (DLS) – AvidNano W130i | CENIMAT Available online: https://www.cenimat.fct.unl.pt/services/laboratory-electronic-and-optoelectronic-materials-and-devices/dynamic-light-scattering-dls-avidnano-w130i (accessed on 9 December 2021).
[28] Austrian SAXS Beamline at Elettra Available online: https://www.elettra.trieste.it/elettra-beamlines/saxs.html (accessed on 9 December 2021).
[29] A.H. Bryk, J.R. Wiśniewski, Quantitative analysis of human red blood cell proteome, J. Proteome Res. 16 (2017) 2752–2761, https://doi.org/10.1021/acs.jproteome.7b00025.
[30] H.K.S. Fye, P. Mrosso, L. Bruce, M.-L. Thézénas, S. Davis, R. Fischer, G.L. Rwegasira, J. Makani, B.M. Kessler, A robust mass spectrometry method for rapid profiling of erythrocyte ghost membrane proteomes, Clin Proteomics 15 (2018) 14, https://doi.org/10.1186/s12014-018-9190-4.
[31] D.S. Gokhin, V.M. Fowler, Feisty Filaments: actin dynamics in the red blood cell membrane skeleton, Curr. Opin. Hematol. 23 (2016) 206–214, https://doi.org/10.1097/MOH.0000000000000227.
[32] B. Machnicka, A. Czogalla, A. Hryniewicz-Jankowska, D.M. Bogusławska, R. Grochowalska, E. Heger, A.F. Sikorski, Spectrins: a structural platform for stabilization and activation of membrane channels, Receptors and Transporters. *Biochim. Biophys. Acta.* 1838 (2014) 620–634, https://doi.org/10.1016/j.bbamem.2013.05.002.
[33] A.J. Baines, Evolution of spectrin function in cytoskeletal and membrane networks, Biochem. Soc. Trans. 37 (2009) 796–803, https://doi.org/10.1042/BST0370796.
[34] A. Czogalla, K. Grzymajło, A. Jezierski, A.F. Sikorski, Phospholipid-induced structural changes to an erythroid beta spectrin ankyrin-dependent lipid-binding site, Biochim. Biophys. Acta. 1778 (2008) 2612–2620, https://doi.org/10.1016/j.bbamem.2008.07.020.
[35] D.M. Bogusławska, B. Machnicka, A. Hryniewicz-Jankowska, A. Czogalla, Spectrin and Phospholipids — the Current Picture of Their Fascinating Interplay, CellMol Biol. Lett. 19 (2014) 158–179, https://doi.org/10.2478/s11658-014-0185-5.
[36] S.E. Lux, Anatomy of the red cell membrane skeleton: unanswered questions, Blood 127 (2016) 187–199, https://doi.org/10.1182/blood-2014-12-512772.
[37] S. Mehboob, B.H. Luo, B.M. Patel, L.W. Fung, Alpha Beta Spectrin Coiled Coil Association at the Tetramerization Site, Biochemistry 40 (2001) 12457–12464, https://doi.org/10.1021/bi010984k.
[38] F. Long, D. McElheny, S. Jiang, S. Park, M.S. Caffrey, L.-W.-M. Fung, Conformational change of erythroid alpha-spectrin at the tetramerization site upon binding beta-spectrin, Protein Sci. 16 (2007) 2519–2530, https://doi.org/10.1110/ps.073115307.
[39] D.-L. Zhang, L.-J. Wu, J. Chen, Y. Liang, Effects of macromolecular crowding on the structural stability of human α-Lactalbumin, Acta. Biochim. Biophys. Sin (Shanghai) 44 (2012) 703–711, https://doi.org/10.1093/abbs/gms052.
[40] M. Ikeguchi, Transient Non-Native Helix Formation during the Folding of β-Lactoglobulin, Biomolecules 4 (2014) 202–216, https://doi.org/10.3390/biom4010202.
[41] J. Mihály, R. Deák, I.C. Szigyártó, A. Bóta, T. Beke-Somfai, Z. Varga, Characterization of Extracellular Vesicles by IR Spectroscopy: fast and simple classification based on amide and CH Stretching Vibrations. *Biochimica et Biophysica Acta (BBA)* -, Biomembranes 1859 (2017) 459–466, https://doi.org/10.1016/j.bbamem.2016.12.005.
[42] S. Berényi, J. Mihály, A. Wacha, O. Tőke, A. Bóta, A mechanistic view of lipid membrane disrupting effect of PAMAM Dendrimers, Colloids Surf. BBiointerfaces 118 (2014) 164–171, https://doi.org/10.1016/j.colsurfb.2014.03.048.
[43] S. Berényi, J. Mihály, S. Kristyán, L. Naszályi Nagy, J. Telegdi, A. Bóta, Thermotropic and Structural Effects of Poly(Malic Acid) on Fully hydrated multilamellar DPPC-water systems, Biochim. Biophys. Acta. 1828 (2013) 661–669, https://doi.org/10.1016/j.bbamem.2012.09.023.
[44] A. Barth, Infrared Spectroscopy of Proteins, Biochim. Biophys. Acta. 1767 (2007) 1073–1101, https://doi.org/10.1016/j.bbabio.2007.06.004.
[45] A. Bóta, A. Wacha, Z. Varga, I.C. Szigyártó, S. Kristyán, A. Lőrincz, P. Szabó, M. Kálmán, L. Naszályi-Nagy, J. Mihály, Role of Oligo(Malic Acid) on the Formation of Unilamellar Vesicles, J. Colloid Interface Sci. 532 (2018) 782–789, https://doi.org/10.1016/j.jcis.2018.08.020.
[46] SasView SasView Available online: https://sasview.github.io/ (accessed on 10 December 2021).
[47] H.G. Mortensen, J.K. Madsen, K.K. Andersen, T. Vosegaard, G.R. Deen, D.E. Otzen, J.S. Pedersen, Myoglobin and α-Lactalbumin Form Smaller Complexes with the Biosurfactant Rhamnolipid Than with SDS, Biophys. J. 113 (2017) 2621–2633, https://doi.org/10.1016/j.bpj.2017.10.024.